Int J Adv Manuf Technol (2018) 95:2301–2313
https://doi.org/10.1007/s00170-017-1275-0

ORIGINAL ARTICLE

Simulation analysis of the influence of dynamic flow stress behavior on chip formation

Linjiang He[1] · **Honghua Su**[1] · **Jiuhua Xu**[1] · **Liang Zhang**[1]

Received: 26 June 2017 / Accepted: 26 October 2017 / Published online: 22 November 2017

Abstract The reliability and accuracy of finite element models of metal machining are heavily reliant on the underlying material flow stress models. The aim of this study is to characterize the relation between the flow stress models and the chip morphology to provide a deeper insight into the process of serrated chip formation. Firstly, in the context of a flow stress model, the critical conditions for generation of the serrated chips are theoretically analyzed. Then, simulations are performed using two different constitutive models with five parameters sets, and the results are discussed in relation to how they verify the theoretical results. In order to better understand the process of serrated chip formation, attention is concentrated on the critical steps characterizing the formation of a single chip segment. The cutting process parameters (stress, strain, and temperature) are discussed. In addition, the mechanism by which the chip morphology transforms from continuous to serrated with increasing cutting speed is investigated in terms of the variation of flow stress curves. The results show that the slope of decrease and the strain value at the peak point of flow stress curves both greatly affect chip morphology. That is, the slope of decrease of the flow stress curve largely controls the formation of serrated chips, while the strain point at the peak determines the frequency and degree of serration of chips. It is found that simulations by manipulating well the flow stress models can produce results for chip morphology, cutting forces, etc. that are closer to those obtained experimentally.

✉ Honghua Su
shh@nuaa.edu.cn

[1] College of Mechanical and Electrical Engineering, Nanjing University of Aeronautics and Astronautics, Nanjing 210016, People's Republic of China

Keywords Finite element simulations · Chip formation · Flow stress behavior · Titanium alloys

1 Introduction

In the aerospace industry, increasing demand for components with critical properties, particularly with regard to their resistance to thermal and mechanical stress, had led to the widespread use of materials such as nickel-based superalloys and titanium alloys, primarily because of their high corrosion resistance, high strength-to-weight ratio, and high temperature strength. However, during machining these materials, serrated chips are normally generated, which are assumed to be the source of the undesirable cutting force vibrations, excessive tool wear, poor surface quality, and poor dimensional accuracy of the machined feature [1–4]. In order to optimize the machining operations and increase tool life, it is necessary to have a deep comprehension of the mechanical processes leading to the formation of serrated chips.

Serrated chip formation has been the subject of a number of investigations using different approaches that have been well documented in several keynote papers [5–7]. Currently, there are three dominant theories for the formation of serrated chips. According to the first of these theories, the serrated chips are generated by the thermoplastic instability, which caused by the localized shear deformation resulting from the predominance of thermal softening over strain hardening. The second proposed mechanism is the crack propagation, which suggests that the serrated chips results from cracks initiating periodically from the free surface of the chip and then propagating to the tool tip. These periodic cracks weaken the primary shear zone leading to catastrophic shear. The third mechanism is the combination of the other two, in which an adiabatic shear band is the precursor to material failure and crack propagation. At

present, there is still significant disagreement about which of these theories provides the best explanation for the serrated chips formation. As analytical or experimental approaches have so far been unable to provide an adequate description of serrated chip formation, researchers have turned to numerical approaches. In particular, finite element modeling has become an important technique in this context [8–10].

The reliability and accuracy of FE models heavily rely on the validity of the underlying flow stress models of working materials in functions of strain, strain rate, and temperature, which requires that all relevant deformation variables during metal cutting be captured in an appropriate constitutive equation [11]. The Johnson-Cook (J-C) model is probably the one that is most widely employed in the finite element analysis of metal cutting processes. It correlates the material flow stress to strain, strain rate, and effects of temperature. However, it is difficult to use the J-C model to simulate the adiabatic shear behavior and the formation of serrated chips that commonly occur when machining nickel-based superalloys and titanium alloys [12]. Moreover, the parameters for the J-C model are usually identified from the non-standardized experimentally determined flow curve fitting techniques, such as the split Hopkinson pressure bar test and the Taylor impact test. The levels of strain, strain rate, and temperature achieved with these experimental techniques are much lower than those encountered during the machining process: a maximum strain of about 50% and a strain rate of around 10^4 s^{-1}, compared with strains in excess of 200% and strain rates of the order of 10^6 s^{-1} during the cutting process [13]. The modeled flow stress can correlate well with the experimental results within the experimental range of strain, strain rate, and temperature. However, it may be considered to be invalid beyond the experimentally studied range, which is extrapolated according to the constitutive equations.

Some attempts have been made to modify the original J-C model or to develop new flow stress models based on the different physical phenomenon and deformation mechanisms. Calamaz et al. [13] developed a Hyperbolic TANgent (TANH) model based on the modified J-C model, which takes into account the strain softening effect through the introduction of the dynamic recovery and recrystallization. At low strains, the flow stress behaves in a similar way as that given by the J-C equation. Beyond a given strain, however, the flow stress decreases until a nearly constant stress is obtained. The TANH model predicts the formation of serrated chip geometrically similar to those observed experimentally. However, although the authors provided the exact values of material parameters for Ti6Al4V alloys, they did not provide the essential information on how to identify the material parameters, especially the modified coefficients. Based on the observations of voids and cracks in the shear band, Rotella and Umbrello [14] developed an energy-based fracture constitutive model in conjunction with grain size evolution equations. In their constitutive model, the Zener-Hollomon (Z-H) equation was used to predict the dynamic recrystallization, while the hardness variations of serrated chips were predicted by incorporating the Hall-Petch (H-P) equation. However, the material parameters of this constitutive model were evaluated by the static material tests, which are not appropriate for modeling the high-strain and high-strain-rate deformation behavior. Zerilli and Armstrong [15] developed the Z-A constitutive model based on the thermal activation theory of dislocations to analyze the dynamic response of metals with Fcc and Bcc microstructure. However, this Z-A constitutive model failed to capture the flow softening phenomenon that is due to dynamic recovery processes at large strain. Liu et al. [16] developed an enhanced Z-A constitutive model by incorporating a material failure function to simulate the adiabatic shear banding that occurs during the machining of Ti6Al4V alloys. The coupling of dynamic recovery with material failure due to void and crack formation results in a flow softening phenomena at high strain. However, these authors calibrated the unknown constants of material model using the machining force data rather than the chip morphology, although it is the latter that is the appropriate characteristic when machining Ti6Al4V alloys. Nemat-Nasser et al. [17] proposed a micromechanical model to include the effect of microstructure dislocation mechanisms and the dynamic strain aging phenomena. The flow stress exhibits a sudden increase at a critical temperature, although it is otherwise monotonically decreasing as a function of increasing temperature. Their results indicated that the thermally activated dislocation motion mechanisms are responsible for adiabatic shear bands. They obtained a good fit to the experimental results by multiplying the stress curves with a temperature coefficient but still provided no suggestion as to how the flow stress could be calculated by extrapolation according to the experimental results.

In summary, despite the many significant achievements that have been made in the development of the flow stress models, there is still a lack of essential details on how to identify the relevant parameters of these flow stress models, especially beyond the experimental range. The underlying cause is that the mechanism on how the flow stress models affect the chip formation process is still a serious issue according to the literatures up to now [18–20]. Moreover, since the flow stress models are of crucial importance for FE approaches to the study of the chip formation mechanism, it is essential to establish appropriate criteria for parameter identification so that the flow stress curves can be better extrapolated and manipulated to provide the simulation results that are closer to the experimental ones.

To fill this gap, the aim of this study is to present a comprehensive and systematic investigation on the influence of flow stress behaviors on the transition motives of chip morphology from continuous to serrated and thereby provide deeper insight into the chip formation process. First, the

correlations between the flow stress behavior and the chip formation process are investigated, and the critical conditions for the flow stress to generate the serrated chip are determined theoretically. Then, orthogonal FE machining models implemented with the TANH constitutive models and the enhanced Z-A models are established. A series of simulations using these models are conducted to verify the theoretical results. The simulation results for cutting forces and chip morphologies are analyzed to characterize the influence of different flow stress curves on the chip formation processes. Finally, the complete segment formation process is considered, and the dynamic cutting process variables (stress, strain, and temperature) are discussed.

2 Theoretical analysis on the mechanism of serrated chip formation

When adiabatic shear instability occurs, the chip morphology transforms from continuous to serrated. Before the onset of adiabatic shear instability, the deformation can be considered as that of continuous chip. The plastic strain ε and strain rate $\dot{\varepsilon}$ in the primary shear zone can be expressed as Eq. 1 and 2 [21].

$$\varepsilon = \frac{\cos\gamma_0}{2\sin\phi\cos(\phi-\gamma_0)} \tag{1}$$

$$\dot{\varepsilon} = \frac{5.9v\sin\phi\cos\gamma_0}{a_c\cos(\phi-\gamma_0)} \tag{2}$$

where γ_0 is the tool rake angle, v is the cutting speed, ϕ is the shear angle, a_c is the undeformed chip thickness.

In the cutting process, the energy needed to prompt the material deformation is converted mostly turns into heat, resulting in an increase in temperature inside the primary shear zone. The work Ws done during the material point deformation is given by Eq. 3.

$$Ws = \int_0^{\varepsilon_0} \sigma\left(\mathrm{P}^{current};\varepsilon,\dot{\varepsilon},T\right)d\varepsilon \tag{3}$$

The heat distribution coefficient ξ is given by Eq. 4 [22].

$$\xi = \frac{1}{1+1.328\sqrt{\frac{\lambda\varepsilon}{va_c}}} \tag{4}$$

where $\lambda = \frac{k_T}{\rho c_0}$ is the thermal conductivity coefficient of the workpiece material, with ρ being the density of workpiece material, k_T the thermal conductivity, and c_0 the heat capacity. As cutting speed increases, the heat distribution coefficient increases due to the time for heat dissipation gets declined. The temperature T in the primary shear zone is defined by Eq. 5 [21, 22]:

$$T = \frac{0.9\xi Ws}{\rho c_0} + T_0 \tag{5}$$

thus the flow stress can be calculated by Eq. 6 (a),

$$\sigma = \sigma_0 \cdot H\left(\varepsilon,\dot{\varepsilon}\right)\cdot S(T,D) \tag{6a}$$

where the coupling effect Ck of hardening effect H and softening effect S can be defined in Eq. 6 (b).

$$Ck = H\left(\varepsilon,\dot{\varepsilon}\right)\cdot S(T,D) \tag{6b}$$

where H is the flow stress hardening effect, which depends mainly on strain and strain rate effect, and S is the flow stress softening effect, which depends mainly on temperature T and other softening factor mechanism, represented here by D. Like the strain softening effect and the material failure effect, D can be related to the strainε.

Figure 1 shows a typical flow stress curve, which can be characterized as several features: SSC (small strain condition), CSZ (Critical strain point zone), QDZ (quick decline zone), and LSC (Large Strain condition). The rate of decrease of the flow stress at large strain k is given by Eq. 7.

$$k = \frac{d\sigma}{d\varepsilon} = \sigma_0 \cdot \frac{d(H\cdot S)}{d\varepsilon} = \sigma_0 \cdot \left[\frac{d(H(\varepsilon,\dot{\varepsilon}))}{d\varepsilon}\cdot S(T,D) + H\left(\varepsilon,\dot{\varepsilon}\right)\cdot\frac{d(S(T,D))}{d\varepsilon}\right] \tag{7}$$

Figure 2 shows the geometry of serrated chip formation process, where S represents the primary shear band. It can be seen that a segment ($B_0B_1C_1C$) is about to be generated and the adiabatic shear sliping occurs along the shear band S. The flow stress in the primary shear band σ_{PSN} and the flow stress

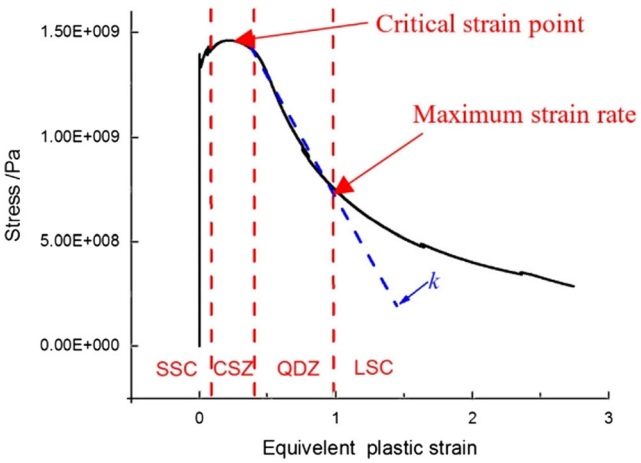

Fig. 1 Typical flow stress curve under thermo-mechanical condition

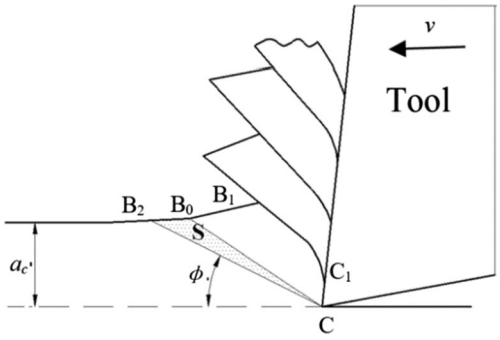

Fig. 2 Geometry diagram of serrated chip formation

adjacent to the shear band σ_{BES} are defined by Eq. 8 (a, b), respectively.

$$\sigma_{PSN} = \sigma_0 \cdot H\left(P^m : \varepsilon_m, \dot{\varepsilon}_m\right) \cdot S(P^m : T_m, D_m)|_{PSN} = \sigma_0 \cdot Ck|_{PSN} \tag{8a}$$

$$\sigma_{ADJ} = \sigma_0 \cdot H\left(P' : \varepsilon', \dot{\varepsilon}'\right) \cdot S\left(P' : T', D'\right)|_{ADJ} = \sigma_0 \cdot Ck'|_{ADJ} \tag{8b}$$

where σ_0 is the initial yield stress, P^m is the variables state of shear band at the maximum strain rate, and P' is the current material state adjacent to the shear band.

When the flow stresses at material points inside the shear band are lower than those of material points adjacent to the shear band, the former points are less able to withstand stress than the latter. As a result, shear slip occurs along the shear band and the serrated chips are expected to generate. This process can be expressed in Eq. 9.

$$\int \sigma\Big|_{ADJ}\left(P' : \varepsilon', \dot{\varepsilon}', T'\right) > \int \sigma\Big|_{PSN}\left(P^m : \varepsilon_m, \dot{\varepsilon}_m, T_m\right) \tag{9a}$$

$$\int H'\left(\varepsilon', \dot{\varepsilon}'\right) \cdot S'\left(T', D'\right) > \int H^m\left(\varepsilon_m, \dot{\varepsilon}_m\right) \cdot S^m(T_m, D_m) \tag{9b}$$

where $P^m(\varepsilon_m, \dot{\varepsilon}_m, T_m)$ represents the deformation state at the maximum strain rate, H^m and S^m are the hardening effect and the softening effect, respectively, $P'\left(\varepsilon', \dot{\varepsilon}', T'\right)$ represent the current state of material points adjacent to the shear band when the material point inside the shear band reach P^m state, ε_m is the strain point at the maximum strain rate.

The adiabatic shear instability inside the shear band S is supposed to occur at the maximum strain rate [19]. Thus, for the flow stress inside the shear band to be lower than that adjacent to it, there must exist a critical rate of decrease k_{cri} of flow stress curve, as expressed in Eq. 10.

$$k = \sigma_0 \cdot \left[\frac{d(H(\varepsilon, \dot{\varepsilon}))}{d\varepsilon} \cdot S(T, D) + H\left(\varepsilon, \dot{\varepsilon}\right) \cdot \frac{d(S(T, D))}{d\varepsilon}\right] > k_{cri}, \quad \varepsilon_c < \varepsilon < \varepsilon_m \tag{10}$$

where $\varepsilon_c$is the strain point at the peak of flow stress curve and ε_m is the strain point at the maximum strain rate.

That is, when the rate of decrease of flow stress is greater than k_{cri}, the softening effect is much stronger than the hardening effect, even at the maximum strain rate. Under this condition, the flow stress, even with much enhanced hardening effect, is still lower than that under small strain. Meantime, the critical strain point must be large enough, such that there is sufficient time for the shearing slipping motion to be initiated and to be developed before the next set of sawtooth material points accumulate to reach their critical state. Consequently, the critical rate of decrease k_{cri} has a negative correlation with the critical strainε_c, as expressed in Eq. 11.

$$k_{cri} = c_1 \cdot \varepsilon_c^{-c_2}, \quad c_2 > 0 \tag{11}$$

where c_1 and c_2 are the coefficients related to the workpiece material and the flow stress models. If the critical strain point is smaller, the rate of decrease of flow stress needs to be larger, which requires that the softening effect be more enhanced than the hardening effect.

In order to better characterize the features of serrated chips, the degree of serration *Gs* and the serration pitch *Lc* of serrated chips were employed. The serration pitch *Lc* is measured as the distance of adjacent segment. The degree of serration *Gs* is defined in Eq. 1 as follows:

$$Gs = \frac{h_2 - h_1}{h_2} \tag{12}$$

where h_2 is the chip segment height and h_1 is the chip root height. For continuous chips, the *Gs* is equal to zero.

For a given cutting condition, the serration pitch *Lc* has a positive correlation with the critical strain pointε_c. That is, if the flow stress model has a smaller critical strain value, it means that materials inside the primary shear band need less plastic deformation length to lead to the plastic instability. Then the serration pitch *Lc* gets smaller and the frequency of serration gets larger. Meanwhile, as the shear slipping motion continues until the ultimate strain value, another sawtooth material has accumulated and reached the critical strain point, which implies that the degree of serration *Gs* is small.

3 FE modeling

An adiabatic two-dimensional finite element modeling of cutting process is proposed. This model is based on the commercial ABAQUS\Explicit, which is suitable for the analysis of the dynamic and highly non-linear processes involving large material deformation. The machining tool is modeled as a rigid body with 3000 elements and the workpiece as isotropic body with 25,000 elements. The initial temperature of workpiece and tool are both set at 20 °C. The cutting tool rake angles is set 3° and the tool

clearance angle α_0 at 7°. The workpiece material is taken as Ti6Al4V alloys, whose flow stress behavior is sufficiently well understood [23–25]. The general thermal and mechanical properties are shown in detail in Table 1 [26]. Given that the cutting time is so short and the thermal conductivity of workpiece material is low, only heat conduction is considered and all the parts faces are assumed to be adiabatic. The boundary conditions of the model are shown in Fig. 3.

3.1 Constitutive models

In finite element analysis, the behavior of workpiece material requires an accurate and reliable material flow stress model. Due to the fact that the hyperbolic TANH model and the enhanced Z-A model have both been highly recommended by many researchers investigating the generation of the serrated chips [13, 16], and have therefore been adopted here, the TANH constitutive model is given by Eq. 13 as follows:

$$\sigma = \left(A + B\varepsilon^{n}\left(\frac{1}{\exp(\varepsilon^{a})}\right)\right)\left(1 + C\ln\frac{\dot{\varepsilon}}{\dot{\varepsilon}_0}\right)\left(1-\left(\frac{T-T_r}{T_m-T_r}\right)^{m}\right)\left(DD + (1-DD)\tanh\left(\frac{1}{(\varepsilon + SS)^{c}}\right)\right) \tag{13}$$

where $DD = 1 - (T/T_m)^d$ and $SS = (T/T_m)^b$, a, b, c, and d are relevant material constants, σ is the equivalent flow stress, ε is the equivalent plastic strain, $\dot{\varepsilon}$ is the equivalent plastic strain rate, $\dot{\varepsilon}_0$ is the reference equivalent plastic strain, T is the current workpiece temperature, and T_m and T_r are the material melting point and room temperature, respectively. The parameters a and c modify the slope of stress-strain decrease at high strains and at relatively low strains (after the pick stress), respectively. The parameter b gives the strain value for which the pick stress is obtained. The parameter d represents the strain softening phenomenon: the higher the value of d, the lower is the magnitude of the strain softening phenomenon.

The enhanced Z-A model is expressed in Eq. 14 as follows:

$$\sigma = \left(A + B\varepsilon^{-(\beta_0-\beta_1\ln\dot{\varepsilon})T} + B_0\sqrt{\varepsilon_r(1-e^{-\varepsilon/\varepsilon_r})}e^{-(\alpha_0-\alpha_1\ln\dot{\varepsilon})T}\right)\cdot\left(h + (1-h)\left(\tanh\left(\frac{a}{\varepsilon}\right)\right)^{kk}\right) \tag{14}$$

where A is the initial flow stress, B, β_0, β_1, α_0, and α_1 are material constants, and ε_r is the characteristic reference strain for dynamic recovery. The failure function is given by the second bracketed term and is controlled by h, a, and kk, which dependent on the strain rate. The parameter h controls the asymptotic value of flow stress at large strains. The parameter a controls the critical strain for initiation of shear band formation. The parameter kk controls the rate of material failure leading to flow softening.

These two constitutive models are implemented into the finite element models by using user subroutines of FORTRAN. The ABAQUS/Explicit software offers an available interface (Vuhard) for users to define the material constitutive models. The user material constitutive model includes the material behavior dependent on field variables or state variables, such as strain, strain rate, and temperature.

Table 1 General thermal and mechanical properties of the workpiece and the cutting tool [26]

Properties	Workpiece	Tool
Density(kg m^{-3})	4430	15,000
Young's modulus(GPa)	113.8	800
Poisson's ratio	0.342	0.2
Thermal expansion(K^{-1})	$8.6e^{-6}$	$4.7e^{-6}$
Melting temperature(K)	1630	–
Thermal conductivity(W m^{-1} K^{-1})	7.3	46
Specific heat capacity(J kg^{-1} K^{-1})	580	203

3.2 Contact and friction behavior

Contact and friction behavior between the workpiece and the cutting tool represents one of the most important and complex aspects of machining processes and has a great effect on the

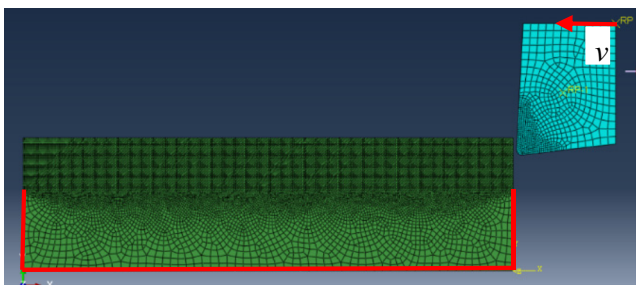

Fig. 3 Boundary conditions of finite element model for orthogonal cutting

cutting forces and chip morphology. In this study, the Coulomb friction law [13] is regarded as the friction model at the tool-chip interface and the value of friction coefficient is assumed to be constant as 0.3. The Coulomb friction law is given by Eq. 15 as follows:

$$\tau = \mu\sigma_n, \text{if} \quad \mu\sigma_n < \overline{m}\frac{\sigma_0}{\sqrt{3}} \tag{15a}$$

$$\tau = \overline{m}\frac{\sigma_0}{\sqrt{3}}, \text{if} \quad \mu\sigma_n > \overline{m}\frac{\sigma_0}{\sqrt{3}} \tag{15b}$$

3.3 Chip separation criteria

In addition, a chip separation criterion was introduced into FE models, which was based on the cumulative value of the equivalent plastic strain at element integration points. The material damage formula is defined by

$$DT = \sum\left(\frac{\Delta\varepsilon^p}{\varepsilon_f}\right) \tag{16}$$

where $\Delta\varepsilon^p$ is the increment of the equivalent plastic strain, ε_f is the equivalent strain at failure, and DT is the damage parameter. When the cumulative equivalent plastic strain reaches the critical strain at failure $\overline{\varepsilon}_f{}^{pl}$, then the damage parameter DT exceeds 1 and the material failure takes place. If all the material failures of integration points take place, the stiffness of the element is set to zero and remains zero for the rest of the calculation. The strain at failure is given by Eq. 17 and the relevant parameters employed in this study are presented in Table 2.

$$\overline{\varepsilon}_f{}^{pl} = \left[d_1 + d_2\exp\left(d_3\frac{p}{q}\right)\right] \times \left[1 + d_4\ln\left(\frac{\dot{\overline{\varepsilon}}^{pl}}{\dot{\varepsilon}_0}\right)\right]\left(1 + d_5\widehat{\theta}\right) \tag{17}$$

where $\overline{\varepsilon}_f{}^{pl}$ is dependent on a non-dimensional plastic strain rate, $\frac{\dot{\overline{\varepsilon}}^{pl}}{\dot{\varepsilon}_0}$, a dimensionless pressure-deviatoric stress ratio, p/q (where p is the pressure stress and q is the Mises stress), and a non-dimensional temperature, θ. Strain at failure is defined by giving the failure parameters d_1–d_5.

In order to better analyze and investigate the influence of flow stress behavior on the chip formation process, the FEM models were calibrated by comparing the simulation results to the experimental ones. The experimental results include cutting forces and chip morphology, as shown in the "Experiments" section. When the numerical model gave results close to the experiments, the FEM models were regarded to be well calibrated and can be used for further analysis and simulations.

Table 2 Failure parameters of chip formation criterion [22]

d_1	d_2	d_3	d_4	d_5
− 0.09	0.25	− 0.05	0.014	3.87

4 Experiments

In order to calibrate the FE models and validate the research results, basic orthogonal cutting tests were conducted on a CNC turning lathe to allow an exact comparison with the 2D FE-simulations, as shown in Fig. 4. A piezoelectric dynamometer (Kistler 9527B) was fixed on the machined table to measure the three-component cutting forces (Fx—the radial force, Fy—the axial force, and Fz—the cutting force). The workpiece material of Ti6Al4V alloy were pretreated to be a series of flat disks, as seen in Fig. 4. Coated (TiAlN) carbide tools with cutting edge length of 3 mm, tool's cutting edge angle of 90°, rake angle of 3°, and the clearance angle of 7° were used in the experiments. The cutting forces signals show that the axial force is equal to zero, which illustrates that the cutting test is strictly orthogonal cutting. The average cutting force is about 180 N and feed force is 70 N. Chips were collected and embeded into epoxy resin to stand on their edge before being mounted and polished straight across their length. They were then etched in 10 ml HF + 20 ml HNO_3 + 300 ml H_2O for 5–10 s for further metallographic examinations. The chip geometries were observed and measured using an optical microscope (Leica DM6M). Experiments showed that machining with a cutting speed of 60 m/min and a feed of 0.1 mm/r gives rise to a serrated chip, as illustrated in Fig. 5b. The maximum and minimum of tooth height are 0.122 and 0.078 mm, respectively. Additionally, it is clearly observed that the grains are highly deformed inside the shear band, with almost undeformed grains inside other zones.

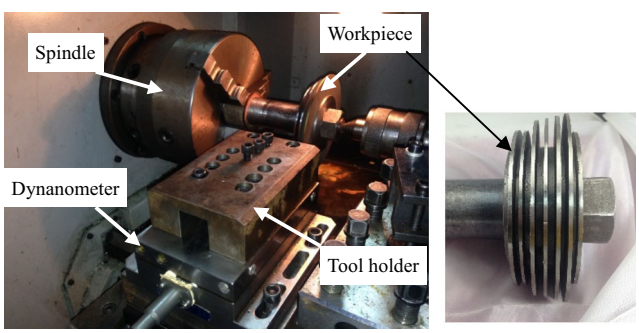

Fig. 4 Orthogonal cutting experimental setup

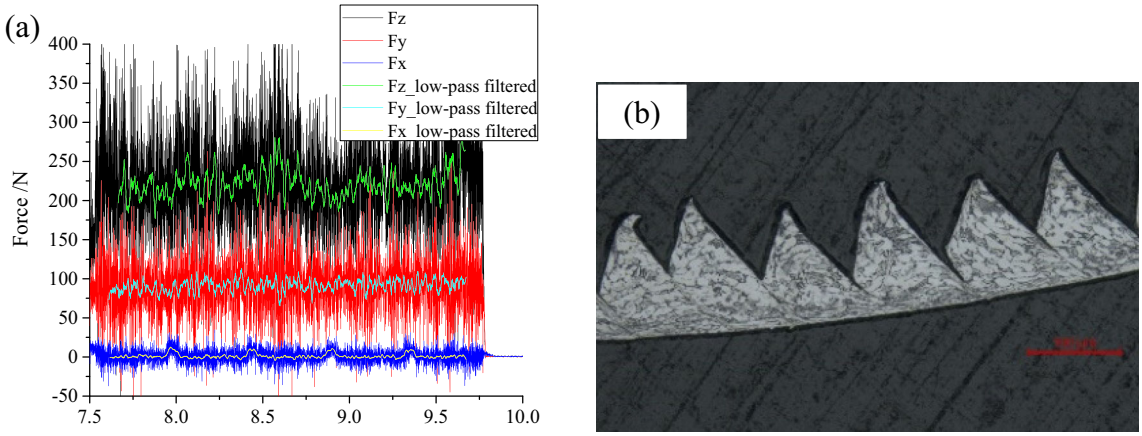

Fig. 5 Experimental results of Ti6Al4V alloys under v = 60 m/min, f = 0.1 mm/r. (**a**) Cutting forces signals. (**b**) Chip morphology

Table 3 Constitutive parameters sets based on the two constitutive models

TANH	*A*(MPa)	*B*(MPa)	*C*	*n*	*m*	*a*	*b*	*c*	*d*
Model 1	1087	1557.7	0.0285	0.82	1.51	1.6	0.4	6.0	1.00
Model 2	1087	1557.7	0.0285	0.82	1.51	1.6	0.4	6.0	4.0
Z-A	*A*(MPa)	*B*(MPa)	β_0	β_1	B_0(MPa)	α_0	*h*	*a*	*kk*
Model 3	690	1485	0.00309	7.47e-5	1135	0.00014	0.2	0.2	6.0
Model 4	690	1485	0.00309	7.47e-5	1135	0.00014	0.2	0.2	2.0
7Model 5	690	1085	0.00309	7.47e-5	1135	0.00014	0.2	0.5	4.0

5 Simulation results and discussion

5.1 Effects of constitutive models on the chip formation

In order to investigate the influence of different flow stress curves on the chip morphology, simulations using several different material constitutive parameter sets were performed for these two constitutive models. The detailed parameters sets are shown in Table 3, which were taken according to the results researched by Calamaz et al. [13] and Liu [16]. These constitutive parameters have been calibrated by the authors according to the experimental results: Models 1 and 2 are being based on the TANH model and Models 3–5 being based on the Z-A model. The parameter *d* of Model 2 is larger than that of Model 1, which suggests that the strain softening effect of Model 2 is much lower than that of Model 1. Thus, the slope of stress-strain decrease in Model 2 is much smoother than that in Model 1. Meanwhile, the parameter *kk* of Model 3 is larger than that of Model 4, which means that the rate of material failure in Model 3 leading to flow softening is larger than that in Model 4. Model 5 is the enhanced Z-A model, which is set to fit the slope of stress-strain decrease of Model 1, but with a lower strain value at peak stress. The flow stress curves are shown in Fig. 6, which are calculated by the Eqs. 13–14 under temperature of 500 °C and strain rate of 1000 s^{-1}. It can be seen that as the strain increases, the flow stresses of all five constitutive models increase sharply to peak at the critical strain points, where ε = 0.4 for the TANH model and ε = 0.2 for the enhanced Z-A model. Then, with increasing strain, the flow stresses of five curves decrease, but with different rates, which is assumed to be a result of the enhanced thermal softening effect coupled with other different softening mechanisms (a strain softening effect or material failure phenomenon). Furthermore, it can be calculated that the maximum rates of decrease of these five models are 2.9×10^9, 8.4×10^8, 2.1×10^{10}, 5.1×10^9, and 1.2×10^9, respectively, and the critical strain values are 0.6, 0.85, 0.22, 0.26, and 0.63, respectively.

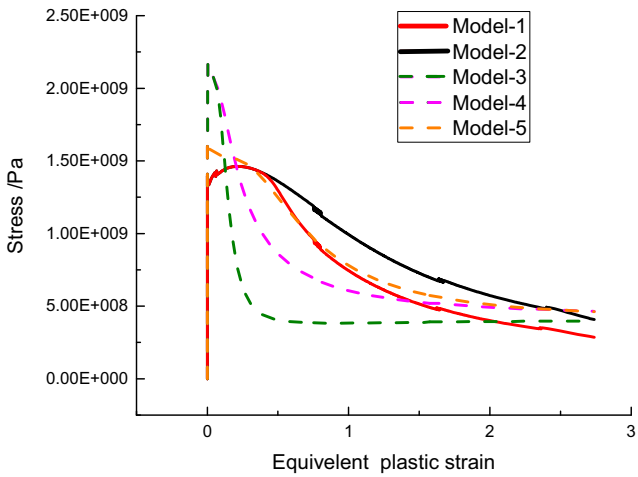

Fig. 6 Flow stress curves based on the two constitutive models

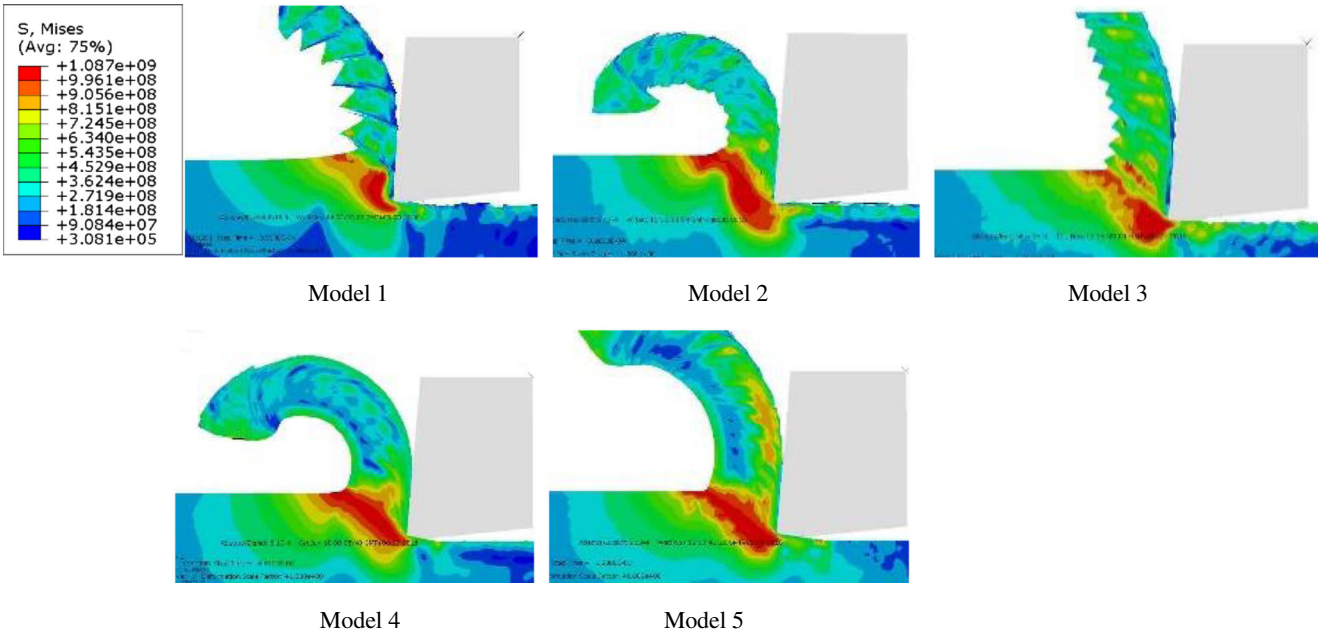

Fig. 7 Chip morphologies under different models (v = 60 m/min, a = 0.1 mm)

Figure 7 shows the chip morphologies obtained from simulations results using these five model sets and the experimental chip morphology. It can be seen that Models 1 and 3 result in serrated chips, while Models 2, 4, and 5 give continuous chips. Considering the differences between the flow stress curves between Models 1 and 2, it can be deduced that the slope of decrease of the flow stress curve largely determines the chip morphology. That is, the greater this slope, the stronger is the tendency for the formation of serrated chips. However, it is worth noting that Model 4 still predicts continuous chips even though it has greater slope of decrease than Model 1, which can be assumed to result from the different strain values at the peak stress. Furthermore, on comparing the chip morphologies in Models 1 and 3, the degree of serration *Gs* of Models 1 and 3 are 0.41 and 0.23, respectively, while the segment pitch *Lc* are 0.107 and 0.036 mm, respectively. It suggests that the frequency of serration for the enhanced Z-A model is much higher than that for the TANH model, while the degree of serration for the enhanced Z-A model is much less than that for the TANH model. This simulation results correlate well with the theoretical analysis. These phenomena suggest that it is not only the slope of decrease of the flow stress curve determines the chip morphology, but also the strain value at peak stress point. It can be deduced that in a

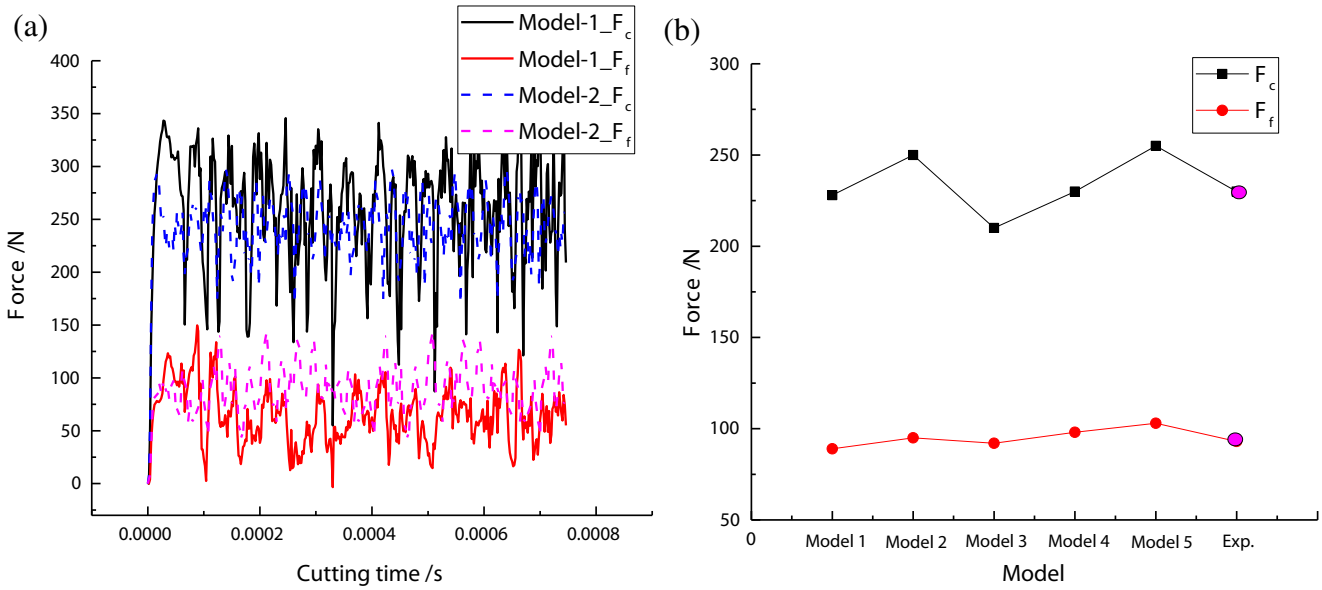

Fig. 8 Simulation cutting forces (v = 60 m/min, a = 0.1 mm). **a** Cutting force signals obtained from simulation. **b** Average forces of five models

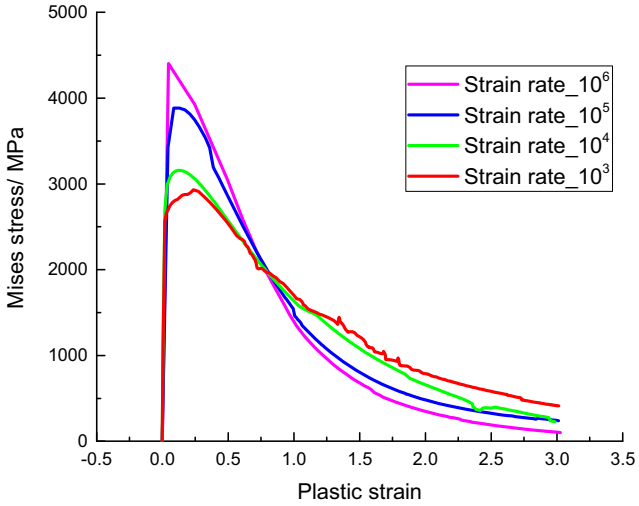

Fig. 9 Variation of von Mises stress curves at different strain rates

constitutive model with a smaller critical strain point, the adiabatic shear state is reached much earlier, which also implies a higher frequency of serration. Meantime, as the sawtooth formation continues until the limit of shearing slip is reached, another sawtooth material has accumulated and reached the critical point for slip. Hence, a small degree of serration can be observed with enhanced Z-A models.

Figure 8a shows the cutting forces signals obtained from simulations using Models 1 and 2, which can be taken to represent the typical cutting forces signals for serrated chips and the continuous chips, respectively. It can be seen that the dynamic cutting forces of serrated chips vary regularly with cutting time, while those of continuous chips fluctuate over a much smaller range, which is assumed to be due to the failure and deletion of the elements during cutting. Figure 8b shows the average cutting forces for the five models, which reveals that the main cutting force in Model 1 is lower than that in Model 2, and the main cutting force in Model 3 is lower than that in Model 4. The feed forces of five models are less than one half the cutting force but exhibit nearly the same trend. It can be then deduced that the higher the flow stress curve, the higher is the cutting force. Thus, if serrated chips with higher cutting forces are found when validating the simulation results with experimental ones, the flow stress curves need to be modified to have higher value of stress while maintaining larger slopes of decrease.

In addition, Fig. 9 shows the flow stress curves for different strain rates with the TANH-based models. As can be seen, increasing the strain rate greatly increases the degree of hardening, which is represented by the higher values of flow stress curves under low-strain conditions. Meanwhile, the greater hardening effect also suggests that more energy is turned into heat, with lower dissipated time, which increases the local temperature rapidly inside the shear band. The thermal softening is also intensified, which is represented by the greater slope of decrease of the flow stress curves. Consequently, it can be deduced that as the cutting speed increases, the strain rate are expected to get larger and the localized shear deformation is more prone to occur; meanwhile, the total work done (the area between the flow stress curve and the axis) during material deformation remains almost unchanged, which means that the cutting forces also remain the same. This correlates well with experimental results on cutting [27].

5.2 Characterizing the variables during the chip formation process

In order to improve understanding of the serrated chip generation process, attention is concentrated here on the typical steps characterizing the formation of a single chip segmentation. Figures 10, 11, and 12, respectively, show the distributions of the equivalent plastic stresses, the equivalent plastic

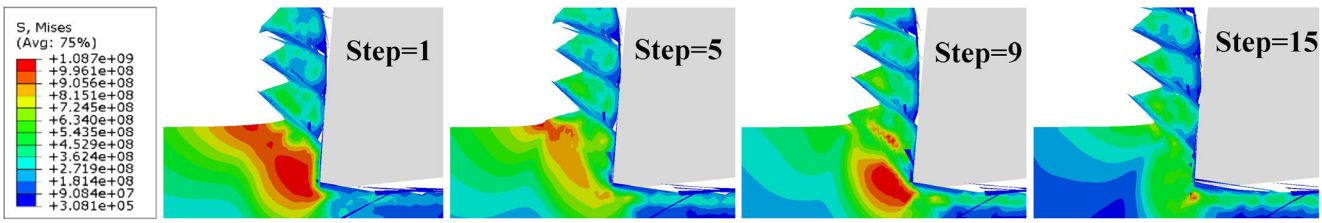

Fig. 10 Distribution of von Mises equivalent stresses during permanent cutting regime (f = 0.1 mm/rev and v = 60 m/min)

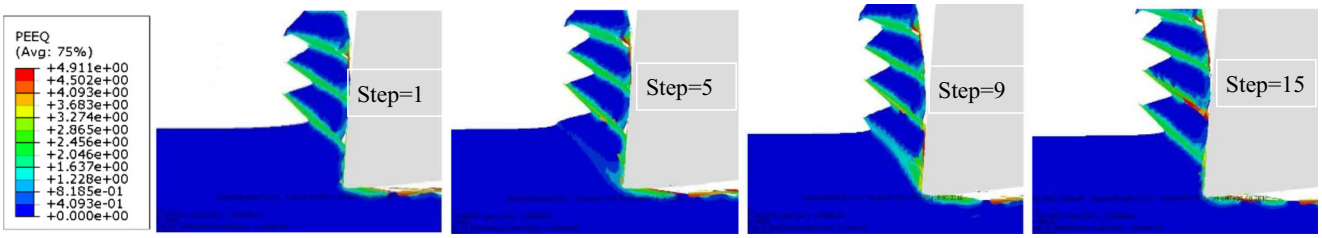

Fig. 11 Distribution of plastic equivalent strain during permanent cutting regime (f = 0.1 mm/rev and v = 60 m/min)

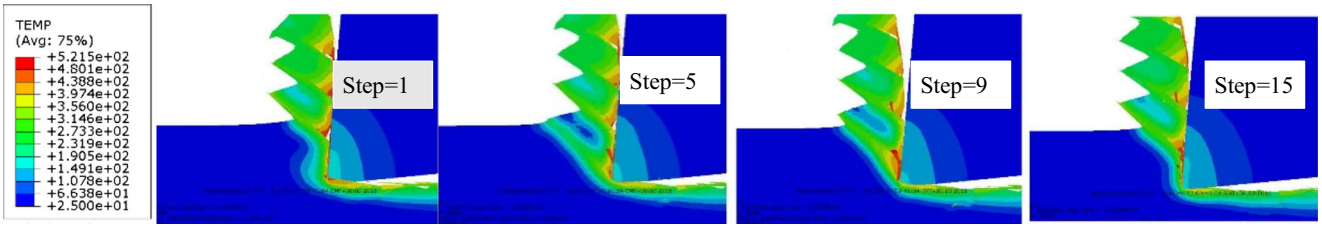

Fig. 12 Distribution of temperature during permanent cutting regime (f = 0.1 mm/rev and v = 60 m/min)

strains, and the temperature during segment generation. As can be seen from Fig. 10, the materials are compressed and bulged ahead of the cutting tool in the initial stage. Meanwhile, an increase in plastic stress can be noted in the primary shear zone. As the cutting tool moves forward, the plastic deformation inside the primary shear zone becomes larger and a considerable amount of plastic deformation work is converted into heat, leading to a rapid increase in temperature inside the primary shear zone. This in turn softens the material in the primary deformation zone, leading to greater deformation. Thus, the flow stress inside the primary shear zone decreases greatly and the thermal plastic instability starts to occur. Meanwhile, it can be clearly be seen that the localized adiabatic shear occurs first near the tool tip and then

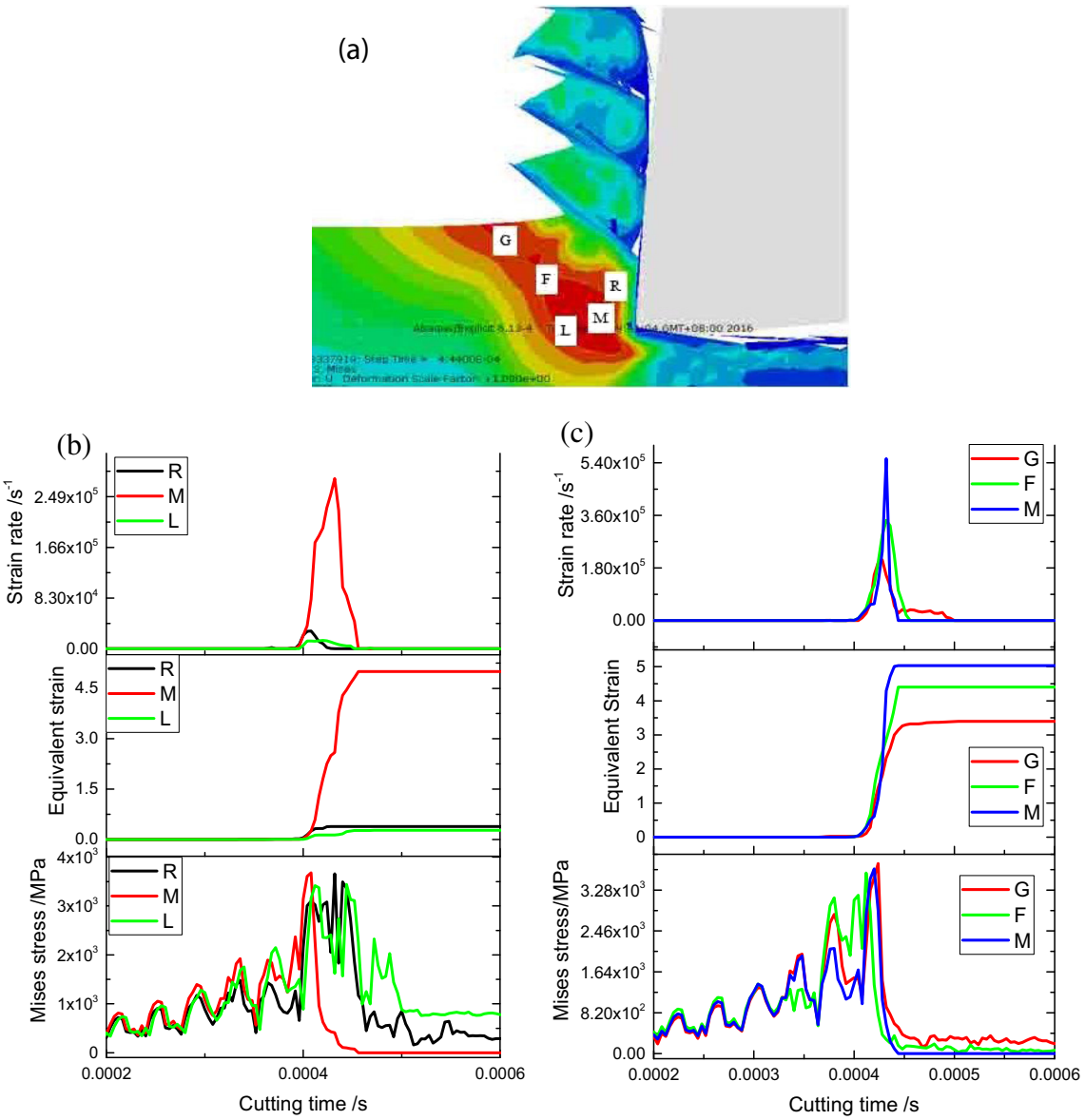

Fig. 13 Variation curves of variable state during the serrated chips formation process

extends toward the free surface of the workpiece, as shown in Figs. 11b and 12b. As the cutting tool continues to move forward, the shear strain increases dramatically, which causes the shear slip to move upward and the localized separation to occur on the free surface of chip, as shown in Fig. 11c. In the final step, the shear slip separation extends along the whole primary shear band owing to the loss in material stiffness.

The variations of plastic strain and flow stress during serrated chip formation process can also be seen by Fig. 13, where the locations of the material critical points R, M, L and G, F, M are given in Fig. 13a. At the beginning, the von Mises stresses of G, F, and M increase gradually with cutting time, and are assumed to be enhanced by elastic deformation, while the plastic strain rate and equivalent plastic strain remain almost zero. When the cutting time reaches the moment at which the flow stress at point M starts to increase sharply to its peak value, the plastic strain increases gradually, while the strain rate increases greatly up to 10^3 s^{-1}. As the cutting time continues to increase, together with the equivalent strain, the strain rate at M increases to 2.4×10^5 s^{-1} and the hardening effect caused by strain hardening and strain rate hardening is greatly enhanced. Once the strain exceeds the critical strain point (0.4), the temperature at G, F, and M increase enormously and the softening effect dominates over the hardening effect, with the result that the flow stress inside the primary shear band decreases rapidly. Meanwhile, the flow stresses at R and L retain higher values because of the effect of elastic/plastic deformation hardening, which in turn subjects the material at G, F, and M to greater deformation, as shown in Fig. 13b. Thus, the localized shear slip occurs, and the serrated chips are generated. Furthermore, it can be seen from Fig. 13c that the plastic shear instability occurs first near the tool tip (point M) and then extends toward the free surface of workpiece.

In the continuous chip formation process, when the material points of chip move into the deformation zone, the flow stresses at G, F, and M increase rapidly to their peak values owing to the hardening effect. They then experience plastic flow with rapid stress relaxation due to material softening, which leads to a loss of bearing capacity of chip material. However, as shown in Fig. 14a, the flow stress at M is still higher than that at R, owing to the fact that the material at G, F, and M experiences a higher strain and strain rate hardening effect, while the softening effect is not so strong. In this situation, it is more difficult for the localized shearing slip to occur along the primary shear zone. Thus, in contrast to the case of shear band instability in primary shear zone in serrated chips formation, the plastic instability of chip flows along the tool rake face occurred in an expanding chip formation zone, resulting in the formation of continuous chips.

The above analysis confirms that the slope of decrease of the flow stress curve and the strain point at the peak largely determine the chip morphology. That is, the slope of decrease of the flow stress curve determines whether the serrated chips are formed, while the strain point at the peak controls the frequency and the degree of serration. If serrated chips are

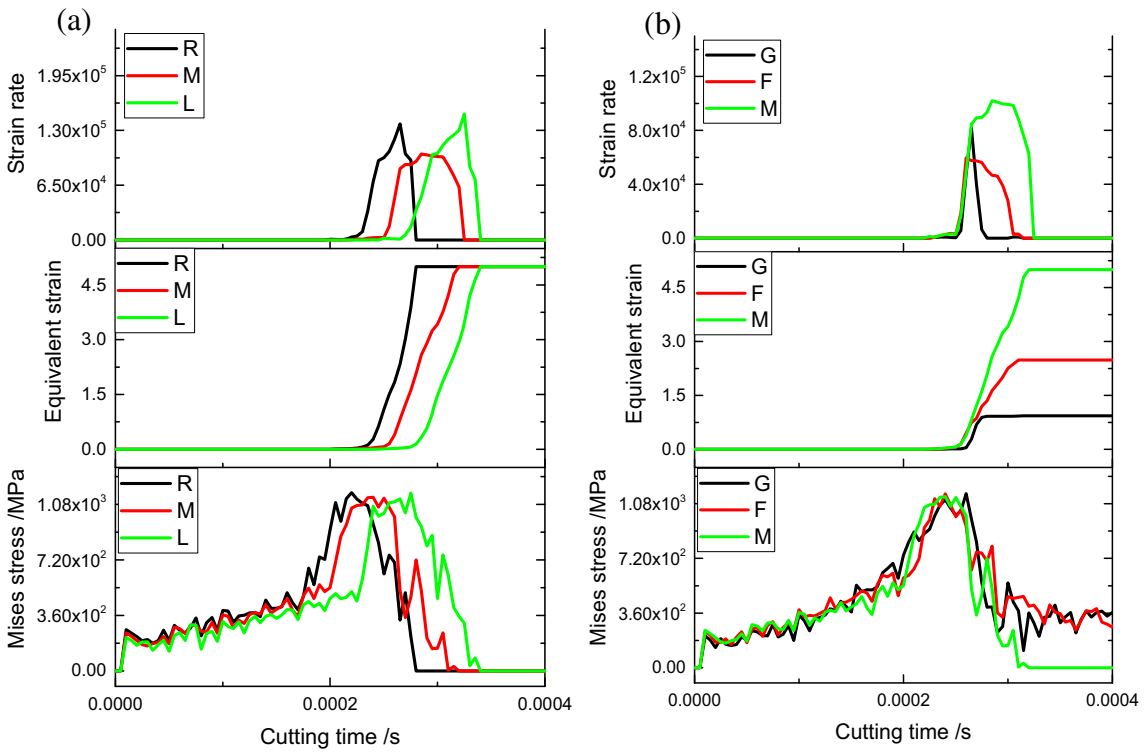

Fig. 14 Variation curves of variable state during continuous chips formation process

found with higher cutting forces when calibrating the FE-machining models against experimental results, then the flow stress curves need to be manipulated to obtain higher stress values while maintaining larger slopes of decrease.

6 Conclusions

This study has investigated the relation between the chip formation process and flow stress model based on finite element analysis. Adiabatic shear band formation has been discussed in the context of the variations in dynamic cutting process variables (strain, strain rate, temperature, and stress), concentrating on the critical stages characterizing the formation of a single serrated chip. Based on an analysis of dynamic flow stress behavior, the present study provides a fundamental understanding of chip formation mechanism that is required for developing more accurate FEM simulations of the machining processes. The main conclusions are drawn as follows:

1. The theoretical analysis has shown that the slope of decrease of the flow stress curve and the critical strain point largely determine the chip morphology. That is, with a greater slope of decrease, it is more likely that serrated chips will be generated, while a smaller critical strain point indicates a higher frequency but a lower degree of serration.
2. Thermal plastic instability occurs first at the tool tip and then extends to the free surface of workpiece along the primary shear zone, which is the necessary condition, but not the only one, for successfully generation of serrated chips. Serrated chips will be generated under circumstances when the flow stress inside the primary shear band is lower than that adjacent to the shear band, so that the chip material can slip along the band.
3. To the best of our knowledge, although previous study have shown that with increasing cutting speed, serrated chips are more likely to be generated for Ti6Al4V alloys, they have not demonstrated the mechanism of this phenomenon. The analysis presented here has shown that with the increasing cutting speed, the strengthened strain rate hardening induces a higher peak value and a greater slope of decrease of flow stress curves, indicating a tendency to generate serrated chips.

Acknowledgements The authors gratefully acknowledge the financial support of the National Natural Science Foundation of China (No.51475233).

References

1. Melkote SN, Liu R, Fernandez Zelaia P, Marusich T (2015) A physically based constitutive model for simulation of segmented chip formation in orthogonal cutting of commercially pure titanium. CIRP Ann Manuf Technol 64(1):65–68
2. Komanduri R, Hou ZB (2002) On thermoplastic shear instability in the machining of a titanium alloy (Ti-6Al-4V). Metall Mater Trans A 33(9):2995–3010
3. Zhang S, Li J, Zhu X, Lv H (2013) Sawtooth chip formation and its effect on cutting force fluctuation in turning of Inconel 718. Int J Precis Eng Man 14(6):957–963
4. Cui XB, Zhao B, Jiao F, Zheng JX (2016) Chip formation and its effects on cutting force, tool temperature, tool stress, and cutting edge wear in high- and ultra-high-speed milling. Int J Adv Manuf Technol 83:55–65
5. Arrazola PJ, Ozel T, Umbrello D, Davies M, Jawahir IS (2013) Recent advances in modelling of metal machining processes. CIRP Ann Manuf Technol 62(2):695–718
6. Wan L, Wang DZ, Gao YY (2016) The investigation of mechanism of serrated chip formation under different cutting speeds. Int J Adv Manuf Technol 82:951–959
7. Wang B, Liu ZQ (2014) Investigations on the chip formation mechanism and shear localization sensitivity of high-speed machining Ti6Al4V. Int J Adv Manuf Technol 75:1065–1076
8. Mahanama M, Movahhedy MR (2012) Application of FEM simulation of chip formation to stability analysis in orthogonal cutting process. J Manuf Process 14(3):188–194
9. Chen G, Ren CZ, Yang XY, Jin XM (2011) Finite element simulation of high-speed machining of titanium alloy (Ti6Al4V) based on ductile failure model. Int J Adv Manuf Technol 56:1027–1038
10. Duan CZ, Zhang LC (2013) A reliable method for predicting serrated chip formation in high speed cutting: analysis and experimental verification. Int J Adv Manuf Technol 64(9–12):1587–1597
11. Sima M, Ozel T (2010) Modified material constitutive models for serrated chip formation simulations and experimental validation in machining of titanium alloy Ti-6Al-4V. Int J Mach Tools Manuf 50(11):943–960
12. Guo YB, Wen Q, Woodbury KA (2006) Dynamic material behavior modelling using internal state variable plasticity and its application in hard machining simulations. J Manuf Sci Eng 128:749–756
13. Calamaz M, Coupard D, Girot F (2008) A new material model for 2D numerical simulation of serrated chip formation when machining titanium alloy Ti-6Al-4V. Int J Mach Tools Manuf 48(3–4): 275–288
14. Rotella G, Umbrello D (2014) Finite element modeling of microstructural changes in dry and cryogenic cutting of Ti6Al4V alloy. CIRP Ann Manuf Technol 63(1):69–72
15. Zerilli FJ, Armstrong RW (1998) Dislocation mechanics based constitutive equation incorporating dynamic recovery and applied to thermomechanical shear instability. AIP Conf Proc:215–218
16. Liu R, Melkote S, Pucha R, Morehouse J, Man X (2013) An enhanced constitutive material model for machining of Ti-6Al-4V alloy. J Mater Process Tech 213(12):2238–2246
17. Nemat-Nasser S, Guo WG, Nesterenko VF, Indrakanti SS, YB G (2001) Dynamic response of conventional and hot isostatically pressed Ti-6Al-4V alloys: experiments and modeling. Mech Mater 33(8):425–439
18. Ducobu F, Riviere-Lorphevre E, Filippi E (2016) Material constitutive model and chip separation criterion influence on the modeling of Ti6Al4V machining with experimental validation in strictly orthogonal cutting condition. Int J Mech Sci 107:136–149
19. Ma W, Chen X, Shuang F (2017) The chip-flow behaviors and formation mechanisms in the orthogonal cutting process of Ti6Al4V alloy. J Mech Phys Solids 98:245–270

20. Mabrouki T, Courbon C, Zhang YC, Rech J, Nelias D, Asad M, Hamdi H, Belhadi S, Salvatore F (2016) Some insights on the modeling of chip formation and its morphology during metal cutting operations. CR Mecanique 344(4–5):335–354
21. Yang Q, Liu Z, Shi Z, Wang B (2014) Analytical modeling of adiabatic shear band spacing for serrated chips in high-speed machining. Int J Adv Manuf Technol 71:1901–1908
22. Tay AO, Stevenson MG, Davis GDV, Oxley PLB (1976) A numerical method for calculating temperature distribution in machining, from force and shear angle measurements. Int J of Mach Tools Design Res 16(4):335–349
23. Ozel T, Yildiz S, Ciurana J (2009) Influence of material models on serrated chip formation in simulation of machining Ti-6Al-4V titanium alloy. Cirp Int Workshop Model Mach Oper San Sebastian, Spain 1:123–130
24. Ducobu F, Riviere-Lorphevre E, Filippi E (2013) Influence of the material behavior law and damage value on the results of an orthogonal cutting finite element model of Ti6Al4V. Procedia CIRP 8: 379–384
25. Wang B, Liu Z (2015) Shear localization sensitivity analysis for Johnson-Cook constitutive parameters on serrated chips in high speed machining of Ti6Al4V. Simul Model Pract Th 55:63–76
26. Ducobu F, Riviere-Lorphevre E, Filippi E (2014) Numerical contribution to the comprehension of sawtoothed Ti6Al4V chip formation in orthogonal cutting. Int J Mech Sci 81:77–87
27. Li PN, Qiu XY, Tang LY (2016) Study on dynamic characteristics of serrated chip formation for orthogonal turning Ti6Al4V [J]. Int J Adv Manuf Technol 86(9):3289–3296